JOURNAL OF COMPUTATIONAL PHYSICS 52, 219–236 (1983)

Birth: A Neutral Beam Deposition Code for Non-Circular Tokamak Plasmas*

M. OTSUKA,† M. NAGAMI, AND T. MATSUDA

Japan Atomic Energy Research Institute, Ibaraki, Japan at the General Atomic Company, San Diego, California

Received July 13, 1982; revised February 8, 1983

A new neutral beam deposition code has been developed which is capable of calculating fast ion deposition profiles including the orbit correction. The code incorporates any injection geometry and a non-circular cross-section plasma with a variable elongation and an outward shift of the magnetic flux surface. Typical CPU time on a KL DEC-10 computer is 10–20 s and 5–10 s with and without the orbit correction, respectively. This is shorter by an order of magnitude than that of other codes, e.g., Monte Carlo beam deposition codes. The power deposition profile calculated by this code is in good agreement with that calculated by the Monte Carlo code which was developed to calculate the complete behaviors of the fast ions in circular plasmas.

1. INTRODUCTION

Many experimental studies to investigate beta limits have recently been carried out in Tokamak devices [1–4]. In these experiments, a high-power neutral beam is injected into the plasma in order to achieve higher beta values. Recent experimental results in the ISX-B [1] and PDX [2] show a decrease in energy confinement time for higher injected beam power. The cause of this decrease is not yet well known. In order to study beam-heated plasmas effectively, it is of primary importance to analyse the data from hundreds of plasma discharges and carefully investigate the parameter dependence of transport phenomena. It is therefore desirable to have a fast data analysis code subject to reasonable simplification. Since one of the most time-consuming elements of the data analysis code for beam-heated plasmas is the calculation of the beam deposition profile for the plasma, it is particularly important to develop a fast beam deposition code in order to analyse the data efficiently.

Several computer codes have been developed to calculate the beam deposition profile for a plasma. Rome [5] developed a computer code for tangential injection into circular plasmas; Fowler [6] developed a Monte Carlo beam deposition code,

† On leave from Hitachi Ltd., Tokyo, Japan.

* This work was performed under a cooperative agreement between the Japan Atomic Energy Research Institute and the United States Department of Energy under DOE Contract No. DE-AT03-80SF11512.

0021-9991/83 $3.00

NFREYA, which was designed for non-circular plasmas. Both codes take the shift of the fast ion drift orbits in the plasma from the magnetic flux surfaces into account. The Monte Carlo beam deposition code is capable of calculating the beam deposition profile for a beam injected with any injection geometry into a plasma which has any configuration of the magnetic flux surfaces. However, from a practical standpoint it is difficult to use the Monte Carlo code as a part of the data analysis code since the Monte Carlo code consumes a great deal of CPU time in order to reduce the statistical error.

Our object here is to develop a fast computer code (less than 1 min KL DEC-10 CPU time per case) which is capable of calculating a beam deposition profile with an orbit correction for a neutral beam injected with any injection geometry into a non-circular Tokamak plasma with displaced magnetic flux surfaces.

Section 2 describes the assumptions and equations employed in the code; Section 3 presents a comparison of the calculated results using the present code with those derived from the Monte Carlo code [12] which was developed to calculate the complete behaviors of the fast ions in circular plasmas and discusses the orbit effect on the beam deposition profile. The summary is presented in Section 4.

2. Calculational Method

2.1. *Assumptions*

The beam deposition code described in this paper has been developed primarily to analyse the data from neutral-beam-heated discharges in the Doublet III Tokamak (a device capable of generating non-circular dee-shaped plasmas with elongations of up to 1.8 [7]). Figure 1(a) shows the magnetic flux contours of a Doublet III plasma

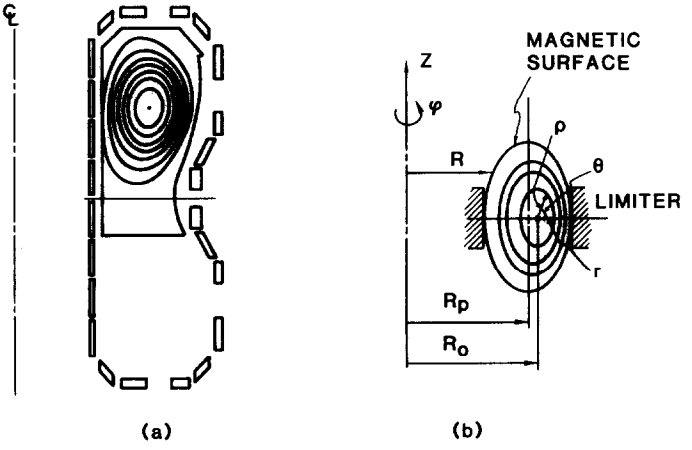

FIG. 1. (a) Magnetic flux contours calculated by the free boundary equilibrium code [8]. (b) Approximated magnetic flux contours employed in the code.

calculated by the free boundary equilibrium code [8]. The outer flux contours are dee-shaped but the inner flux contours ($r < \frac{2}{3}a$) (the region in which the transport phenomenon is important because the hot plasma is contained in this region) have elliptical shapes with variable elongations. The flux contours are not all concentric but shift outward and this shift becomes larger in high beta plasmas. These features are common to non-circular dee-shaped plasmas. Because of these considerations, in order to simplify the calculation the magnetic flux contours are approximated as ellipses with variable elongations and outward shifts both of which depend on the plasma minor radius.

In general, the beam deposition profile can be simply calculated with a so-called pencil beam approximation. However, with this approximation the beam deposition profile diverges near the point at which the injected beam is tangent to the magnetic flux surface. In the present code, the so-called diffused beam which has a finite beam radius is considered to eliminate the divergence and the beam cross-sectional shape is approximated as ellipse.

This approximation is quite reasonable since almost all the neutral beams extracted from several types of ion source have a circular or elliptical cross sectional shape. The beam current density is constant for each concentric ellipse and depends only on the radius of this ellipse. The neutral beam usually has a divergence angle of 1–2°. In this code, the beam divergence is neglected, i.e., the parallel beam is considered because of the expansion of the beam radius in the plasma due to the beam divergence being negligibly small in comparison to the beam radius itself.

Drift orbits of fast ions created in the plasma by ionization and charge exchange are divided into two groups, transit orbit and banana orbit. In general, the fast ions distribute non-uniformly in both the poloidal and toroidal direction, especially when the fast ions move along the banana orbits. However, from the viewpoint of energy transfer to the plasma from the fast ions, it is a reasonable approximation that the fast ions distribute uniformly in both the poloidal and toroidal direction and that their birth rates depend only on the minor radius of the magnetic flux contour since the plasma ions and electrons move uniformly on the magnetic flux surface in which the fast ions transfer their energy to the plasma through classical coulomb collisions.

The shift of the fast ion drift orbits from the magnetic flux contour is ~2–5 cm in Doublet III for the transit orbits; the banana width is ~5–10 cm for banana orbits under typical experimental conditions (plasma current: 300 kA–1 MA, beam energy: 60–80 keV). These shifts and widths although not very large cannot be neglected, especially in the case of a near-perpendicular injection as in Doublet III, since a large number of fast ions move along the banana orbits for the near-perpendicular injection. Therefore, in the present code this orbit effect is taken into account in the following manner. A fast ion created on a magnetic flux surface moves along a particular orbit crossing the magnetic flux surfaces. The fast ion deposition profile is then weighted by the fraction of bounce time which the fast ion spends in each differential volume between the magnetic flux surfaces.

The fast ions usually diffuse across the magnetic flux surfaces due to pitch angle scattering during the slowing down process. However, this spatial diffusion of fast

ions can be neglected for all practical purposes since the characteristic time of pitch angle scattering is long compared to the typical slowing-down time in many cases of neutral-beam-heating experiments. The calculated results given by the Monte Carlo code [12] show that this diffusion can be neglected. (See Section 3.2.)

2.2. *Equations*

2.2.1. *Magnetic flux contours*

Each magnetic flux contour calculated by the free boundary equilibrium code is approximated as an ellipse which is shown in Fig. 1(b), and then expressed by the following equations in cylindrical coordinates (R, ϕ, z).

$$\begin{aligned} (R - R_0(X))^2 + z^2 &= \rho^2, \\ R &= R_0(X) + \rho \cos\theta, \\ z &= \rho \sin\theta. \end{aligned} \tag{1}$$

$R_0(X)$ is expressed by

$$R_0(X) = R_p + \Delta(X). \tag{2}$$

The relation between ρ and θ is given by

$$\frac{\rho^2}{r^2}\left(\cos^2\theta + \frac{1}{\kappa(X)^2}\sin^2\theta\right) = 1, \tag{3}$$

where r is the minor radius of the magnetic flux contour in the midplane, $X = r/a$, a is the plasma minor radius (i.e., the minor radius of the outermost magnetic flux contour), $\kappa(X)$ is the elongation, R_p is the plasma major radius (i.e., the major radius of the outermost magnetic flux contour), $\Delta(X)$ is the outward shift of the magnetic flux contour and $R_0(X)$ is the major radius of the magnetic flux contour. $\kappa(X)$ and $\Delta(X)$ are approximated with the appropriate functions so that they fit the calculated ones by the equilibrium code.

$$\kappa(X) = C_{k1} + C_{k2}X^2 + C_{k3}X^4, \tag{4}$$

$$\frac{\Delta(X)}{a} = C_{d1} + C_{d2}X^2 + C_{d3}X^4, \tag{5}$$

where C_{k1}, C_{k2}, C_{k3}, C_{d1}, C_{d2} and C_{d3} are constants.

The toroidal plasma volume, $V(r)$, enclosed by an magnetic flux surface is expressed by

$$V(r) = \pi r^2 \kappa(X) \cdot 2\pi R_0(X). \tag{6}$$

Therefore, the differential volume, $dV(r)$, between the magnetic flux surfaces is expressed by

$$dV(r) = 2\pi^2 r\, dr \left(2\kappa(X) \cdot R_0(X) + X \frac{d\kappa(X)}{dX} R_0(X) + X \cdot \kappa(X) \frac{dR_0(X)}{dX}\right). \quad (7)$$

2.2.2. *Fast ion deposition profile*

In this section, the fast ion deposition profile without the orbit correction is described. The fast ions created on any magnetic flux surface distribute uniformly on this surface. In this case, the fast ion birth rate at a minor radius in the midplane of r, due to a small beam element injected into the plasma, is calculated by dividing the number of fast ions created between a magnetic flux surface of the minor radius, r, and the minor radius, $r - dr$, with the differential volume between these surfaces (see Fig. 2). That is, the fast ion birth rate due to a small beam element, $d\dot{n}_B(r)$, is given by

$$d\dot{n}_B(r) = \frac{1}{dV(r)} \cdot ds \cdot (R_0 + \rho \cos\theta)\, d\phi\, |\mathbf{e}_n \cdot \mathbf{e}_l|\, J(\rho, \theta, \phi) \cdot dl \cdot n_e(r) \cdot \bar{\sigma}_t(r), \quad (8)$$

where $n_e(r)$ and $\bar{\sigma}_t(r)$ are the electron density and the total ionization cross section at the minor radius of r, respectively, $\mathbf{e}_n$ is the normal vector of the magnetic flux surface at the point (ρ, θ, ϕ) and $\mathbf{e}_l$ is the unit vector in the direction of injection. Here, $J(\rho, \theta, \phi)$ is the neutral beam current density at the point (ρ, θ, ϕ) on the magnetic flux surface and is expressed by

$$J(\rho, \theta, \phi) = J_0(\rho, \theta, \phi) \exp\left\{-\int_{l_p(\rho,\theta,\phi)}^{l(\rho,\theta,\phi)} n_e(r)\, \bar{\sigma}_t(r)\, dl\right\}, \quad (9)$$

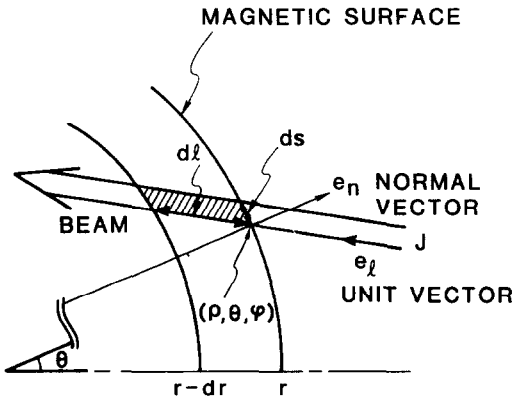

FIG. 2. Description of calculational model for the fast ion birth rate due to a small beam element.

where $J_0(\rho, \theta, \phi)$ is the neutral beam current density on the outermost magnetic flux surface before attenuating, $l_p(\rho, \theta, \phi)$ is the distance from an intersecting point of the beam element and the (x, z) plane to the point at which the beam element crosses the outermost magnetic flux surface and $l(\rho, \theta, \phi)$ is the distance from the intersecting point to the point (ρ, θ, ϕ).

The total fast ion birth rate due to the total neutral beam injected into the plasma is given by integrating Eq. (8) inside the region on the magnetic flux surface defined as the intersectional area of the neutral beam and the magnetic flux surface.

$$\dot{n}_B(r) = \frac{n_e(r)\,\bar{\sigma}_i(r)}{2\pi^2 r\left(2\kappa R_0 + X\frac{d\kappa}{dX}R_0 + X\kappa\frac{dR_0}{dX}\right)} \times \int_{\theta_a}^{\theta_b}\int_{\phi_a(\theta)}^{\phi_b(\theta)} \frac{ds(R_0+\rho\cos\theta)\,d\phi\,|\mathbf{e}_n\cdot\mathbf{e}_l|\cdot J(\rho,\theta,\phi)}{\left|\frac{dr}{dl}\right|}. \tag{10}$$

The intersectional area and the limits of the integral in Eq. (10) are shown in Fig. 3.

Figure 4 shows the injection geometry in a cartesian coordinate system anchored in the center of the torus. The point $(x_0, 0, z_0)$ defined on the (x, z) plane is the cross point of the beam center line and the (x, z) plane. θ_1 is the angle between the x axis and the unit vector, $\mathbf{e}_l$, in the direction of the injection projected on the (x, y) plane. θ_2 is the angle between the unit vector, $\mathbf{e}_l$, and the (x, y) plane. The orbit of the beam element parallel to the beam center line is expressed by

$$\begin{aligned} x &= x_s - l\cos\theta_2\cos\theta_1, \\ y &= l\cos\theta_2\sin\theta_1, \\ z &= z_s - l\sin\theta_2, \end{aligned} \tag{11}$$

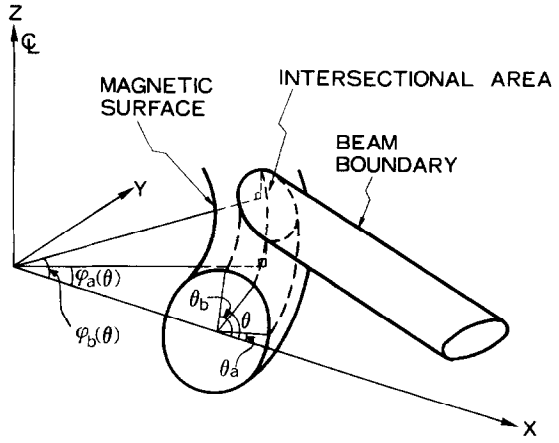

FIG. 3. Intersectional area of the neutral beam and a magnetic flux surface.

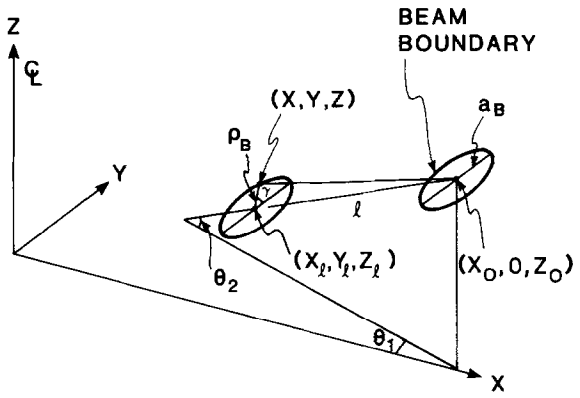

FIG. 4. Injection geometry and notation of variables.

where l is the distance from the intersecting point $(x_s, 0, z_s)$ of the beam element and the (x, z) plane to a point (x, y, z). The relation between the minor radius, r, and the distance, l, is obtained from Eqs. (3) and (11) using $x = (R_0 + \rho \cos\theta)\cos\phi$ and $y = (R_0 + \rho\cos\theta)\sin\phi$.

$$r^2 = \frac{1}{\kappa(X)^2}(z_s - l\sin\theta_2)^2 + \{(l^2\cos^2\theta_2 + x_s^2 - 2x_s\, l\cos\theta_2\cos\theta_1)^{1/2} - R_0(X)\}^2; \tag{12}$$

dr/dl in Eq. (10) is then obtained by differentiating Eq. (12) by r,

$$\frac{dr}{dl}\left(r + \frac{\rho^2\sin^2\theta}{\kappa^3\cdot a}\cdot\frac{d\kappa}{dX} + \frac{\rho\cos\theta}{a}\cdot\frac{dR_0}{dX}\right) = \rho\cos\theta\cos\theta_2(\sin\phi\sin\theta_1 - \cos\phi\cos\theta_1) - \frac{1}{\kappa^2}\rho\sin\theta\sin\theta_2. \tag{13}$$

The unit vector, $\mathbf{e}_l$, and the normal vector $\mathbf{e}_n$, are expressed by

$$\mathbf{e}_l = (-\cos\theta_2\cos\theta_1, \cos\theta_2\sin\theta_1, -\sin\theta_2), \tag{14}$$

$$\mathbf{e}_n = \left\{-\left(\frac{\partial\rho}{\partial\theta}\sin\theta + \rho\cos\theta\right)\cos\phi\frac{d\theta}{ds}, -\left(\frac{\partial\rho}{\partial\theta}\sin\theta + \rho\cos\theta\right)\sin\phi\frac{d\theta}{ds}, \left(\frac{\partial\rho}{\partial\theta}\cos\theta - \rho\sin\theta\right)\frac{d\theta}{ds}\right\}. \tag{15}$$

Thus,

$$|\mathbf{e}_n\cdot\mathbf{e}_l| = |H|\frac{d\theta}{ds}, \tag{16}$$

where

$$H = \left(\frac{\partial \rho}{\partial \theta}\sin\theta + \rho\cos\theta\right)\cos\phi\cos\theta_2\cos\theta_1 - \left(\frac{\partial \rho}{\partial \theta}\sin\theta + \rho\cos\theta\right)\sin\phi\cos\theta_2\sin\theta_1 - \left(\frac{\partial \rho}{\partial \theta}\cos\theta - \rho\sin\theta\right)\sin\theta_2. \quad (17)$$

Finally, the following equation is obtained by substituting Eq. (16) in Eq. (10):

$$\dot{n}_B(r) = \frac{n_e(r)\,\bar{\sigma}_t(r)}{2\pi^2 r(2\kappa R_0 + X(d\kappa/dX)\,R_0 + X\kappa(dR_0/dX))} \times \int_{\theta_a}^{\theta_b}\int_{\phi_a(\theta)}^{\phi_b(\theta)} \frac{d\theta\,d\phi(R_0+\rho\cos\theta)\,|H|\,J(\rho,\theta,\phi)}{|dr/dl|}. \quad (18)$$

2.2.3. *Intersection of the neutral beam and the magnetic flux surface*

The cross-sectional shape of the neutral beam is approximated as an ellipse whose axis is parallel to the (x, y) plane. In this case, the boundary surface of the neutral beam is given by the following equations with notations in Fig. 4:

$$\begin{aligned}
&(x-x_0)^2 + y^2 + (z-z_0)^2 = l^2 + \rho_B^2,\\
&l = -(x-x_0)\cos\theta_2\cos\theta_1 + y\cos\theta_2\sin\theta_1 - (z-z_0)\sin\theta_2,\\
&\frac{\rho_B^2}{a_B^2}\left(\cos^2\gamma + \frac{1}{\kappa_B^2}\sin^2\gamma\right) = 1,\\
&\rho_B\cos\gamma = (x-x_l)\sin\theta_1 + (y-y_l)\cos\theta_1,\\
&x_l - x_0 = -l\cos\theta_2\cos\theta_1,\\
&y_l = l\cos\theta_2\sin\theta_1,
\end{aligned} \quad (19)$$

where a_B is the length of the ellipse axis parallel to the (x, y) plane, κ_B is the ellipticity and ρ_B is the radius of the ellipse.

The intersection is calculated by substituting Eq. (3), $x = (R_0 + \rho\cos\theta)\cos\phi$ and $y = (R_0 + \rho\cos\theta)\sin\phi$ in Eq. (19). The fast ion birth rate on any magnetic flux surface is then given by integrating Eq. (18) inside the obtained intersectional area.

2.2.4. *Ionization cross section*

The neutral atoms injected into the plasma are ionized through electron impact ionization, ion impact ionization and charge exchange. The electron impact ionization cross section, the hydrogenic ion impact ionization cross section and the charge exchange cross section with hydrogenic ions are well known and calculated from formulas given by Riviere [9]. The impurity ion impact ionization cross section and charge exchange cross section with the impurity ions in the plasma are described as

$\sigma_{iz} = Z^{1.4}(\sigma_{ii} + \sigma_{cx})$ by Olson [10]. Here, σ_{iz} is the total electron loss cross section with the impurity ions, Z is the charge number of the impurity ions, σ_{ii} is the proton impact ionization cross section, and σ_{cx} is the charge exchange cross section with protons. In order to calculate the total electron loss cross section with the impurity ions, it is necessary to know the charge numbers and density of all kinds of impurity ions. However, at the present time, it is impossible in practice to have this information. Therefore, in the present code we assume that there is one species of impurity ion whose charge number is Z and that the effective charge number, Z_{eff}, is spatially uniform. Under these assumptions, the total electron loss cross section is expressed by

$$\bar{\sigma}_t(r) = \bar{\sigma}_{ie}(r) + (\bar{\sigma}_{ii}(r) + \bar{\sigma}_{cx}(r))\{f + (1-f)^{0.6} \cdot (Z_{eff} - f)^{0.4}\}, \tag{20}$$

$$f \equiv \frac{n_i(r)}{n_e(r)} = \frac{Z - Z_{eff}}{Z - 1}, \tag{21}$$

where $\bar{\sigma}_t(r)$ is the total electron loss cross section averaged over the Maxwellian distribution, $\bar{\sigma}_{ie}(r)$ is the electron impact ionization cross section averaged over the Maxwellian distribution of electrons at the local electron temperature, $\bar{\sigma}_{ii}(r)$ and $\bar{\sigma}_{cx}(r)$ are the proton impact ionization cross section and charge exchange cross section with protons averaged over the Maxwellian distribution of ions at the local ion temperature, respectively, and $n_i(r)$ is the plasma ion density. In the present code, the temperature and density profile in the plasma can be approximated with the appropriate functions (see Eqs. (33) and (34)).

2.2.5. *Orbit correction*

In the cylindrical coordinate system shown in Fig. 1(b), the drift orbits of the fast ions are calculated according to the following equation under the assumption that the magnetic field is static and axisymmetric and that the toroidal magnetic field is larger than the poloidal magnetic field [11].

$$\psi + \frac{2\pi m}{e} v_{||} R = \text{const}, \tag{22}$$

where ψ is the poloidal magnetic field flux and m, e, and $v_{||}$ are the mass, the charge, and the guiding center velocity of the fast ions parallel to the axisymmetric magnetic field, respectively.

Equation (22) is independent of the ϕ-direction because of the assumption of axisymmetry. Thus, the fast ion drift orbit defined by Eq. (22) represents the projection of the drift orbit onto the (R, z) plane. Furthermore, we may calculate the drift orbit on only the half-plane over the horizontal line since the plasma is symmetric against the horizontal line.

The magnetic moment and the kinetic energy of the fast ion are conserved under the assumptions of a small variation in the magnetic field within the area of the Larmor radius and in the gyration time of the fast ions as well as less collisions and the lack of an electric field in the plasma.

Equation (22) can be rewritten by using these assumptions.

$$\psi(R, z) + \alpha \frac{2\pi m v}{e} \{R(R - R^*)\}^{1/2} = K(R, z, R^*), \tag{23}$$

where $R^* \equiv R_b v_{\perp b}^2 / v^2$, R_b is the major radius where the fast ion is created, $v_{\perp b}$ is the fast ion velocity perpendicular to the magnetic field at the birth point of the fast ion, v is the fast ion velocity, and $\alpha = 1$ or -1 when $v_{||}$ is in the same or opposite direction as the plasma current. $K(R, z, R^*)$ in Eq. (23) is the constant determined by the fast ion birth point and the related pitch angle. $\psi(R, z)$, required to solve Eq. (23), is given by calculating the free boundary equilibrium code [8] for each plasma discharge and is approximated as an appropriate polynomial function which depends only on the minor radius of the magnetic flux contour which is approximated as the ellipse given by Eq. (3) according to the equilibrium calculation. That is,

$$\psi(X) = C_{p0} + C_{p2} X^2 + C_{p3} X^3 + C_{p4} X^4, \tag{24}$$

where C_{p0}, C_{p2}, C_{p3}, and C_{p4} are constants. The magnetic flux contour is rewritten in the cylindrical coordinate system shown in Fig. 1(b) by

$$(R - R_0(X))^2 = r^2 - \frac{z^2}{\kappa(X)^2} \tag{25}$$

This approximation described above for the poloidal magnetic flux simplifies the calculation of the fast ion drift orbits and consequently reduces the CPU time for the calculation of the orbit correction significantly.

The fast ion drift orbit is calculated by solving Eq. (23) using Eqs. (24) and (25). The fast ion deposition profile with the orbit correction is obtained by weighting each fast ion birth rate by the fraction of bounce time which the fast ion spends in the related differential volume between the magnetic flux surfaces. The fast ion birth rate at the minor radius of r_i, $\Delta \dot{n}_B(r_i)$, which originates from the fast ion created on the magnetic flux surface of the minor radius, r_j, is expressed by

$$\Delta \dot{n}_B(r_i) = d\dot{n}_B(r_j) \cdot dV(r_j) \cdot W_{ij}(\rho_j, \theta_j, \phi_j, r_i, r_j) \cdot dr_i \cdot \frac{1}{dV(r_i)}, \tag{26}$$

where $d\dot{n}_B(r_j)$ given by Eq. (8) is the fast ion birth rate due to a small beam element, $dV(r_i)$ and $dV(r_j)$ are differential volumes at the minor radii of r_i and r_j, respectively, and $W_{ij}(\rho_j, \theta_j, \phi_j, r_i, r_j)$ is the fraction of bounce time which the fast ions created at the point $(\rho_j, \theta_j, \phi_j)$ on the magnetic flux surface of the minor radius, r_j, spend in the unit length of the minor radius at the minor radius of r_i. The total fast ion birth rate with the orbit correction at the minor radius of r_i is obtained by integrating Eq. (26) with θ_j, ϕ_j, and r_j using Eqs. (7) and (8).

$$\dot{n}_B(r_i) = \frac{1}{2\pi^2 r_i(2\kappa(X_i)R_0(X_l) + X_i(d\kappa(X_i)/dX)R_0(X_i) + X_l \cdot \kappa(X_i)(dR_0(X_i)/dX))}$$

$$\times \int_{r_1(r_i)}^{r_2(r_i)} dr_j \int_{\theta_\alpha(r_j)}^{\theta_\beta(r_j)} d\theta_j \int_{\phi_\alpha(\theta_j)}^{\phi_\beta(\theta_j)} d\phi_j \frac{1}{|dr_j/dl|} \tag{27}$$

$$\times \{n_e(r_j)\bar{\sigma}_l(r_j)(R_0 + \rho_j \cos\theta_j)\,|H_j| \cdot J(\rho_j, \theta_j, \phi_j) \cdot W_{ij}(\rho_j, \theta_j, \phi_j, r_i, r_j)\}.$$

Fast ions which are able to travel across the magnetic flux surface at the minor radius, r_i, are created inside the area surrounded by $\theta_\alpha(r_j) - \theta_\beta(r_j)$ and $\phi_\alpha(\theta_j) - \phi_\beta(\theta_j)$ on the magnetic flux surface of the minor radius, r_j, and also created between the minor radius, $r_1(r_i)$ and $r_2(r_i)$.

The bounce time, τ, which the fast ion spends in the differential volume between the magnetic flux surfaces of the minor radius, r and r', is given by

$$\tau = \int_r^{r'} \frac{(dR^2 + dz^2)^{1/2}}{(v_R^2 + v_z^2)^{1/2}}, \tag{28}$$

where $(dR^2 + dz^2)^{1/2}$ is an element of arc length in the drift orbit on the (R, z) plane, v_R and v_z are the R-component and the z-component of the fast ion velocity, respectively, expressed by the following equations under the assumption that the toroidal magnetic field is larger than the poloidal magnetic field.

$$v_R = \frac{v_{||}}{B} \cdot \frac{1}{2\pi R} \frac{\partial \psi}{\partial z}, \tag{29}$$

$$v_z = \alpha \frac{v_{||}}{B} \cdot \frac{1}{2\pi R} \frac{\partial \psi}{\partial R} + \frac{m}{2eBR}(2v^2 - v_\perp^2), \tag{30}$$

where $v_{||} = v(1 - R^*/R)^{1/2}$.

The fraction of the bounce time, W_{ij}, is given by

$$W_{ij}(\rho_j, \theta_j, \phi_j, r_i, r_j) = \frac{\tau(\rho_j, \theta_j, \phi_j, r_i, r_j)}{\tau_t(\rho_j, \theta_j, \phi_j, r_j)}, \tag{31}$$

where $\tau_t(\rho_j, \theta_j, \phi_j, r_j)$ is the bounce time with which the fast ion created at the point $(\rho_j, \theta_j, \phi_j)$ on the magnetic flux surface of the minor radius, r_j, travels along the entire length of its orbit and $\tau(\rho_j, \theta_j, \phi_j, r_i, r_j)$ is the bounce time which the same fast ion spends in the unit length of the minor radius at the minor radius of r_i.

3. Typical Calculational Results

The fast ion deposition profile is obtained by integrating Eq. (18) or Eq. (27) numerically. The integral of Eq. (18) without the orbit correction is performed by the

following procedure. First, an intersectional area of the neutral beam and a magnetic flux surface is divided into meshes in both the poloidal and toroidal direction and an orbit for a small beam element which passes each mesh point is calculated. Second, the neutral beam current density at each mesh point is calculated by using Eq. (9) and the fast ion birth rate due to the small beam element is calculated. Finally, the integral is performed by summing the fast ion birth rates at all mesh points inside the intersectional area. In this step, Gaussian integration is employed in order to reduce the computational time.

The integral of Eq. (27) with the orbit correction is performed using almost the same procedure described above except for the following step. The fast ion birth rate at each mesh point on a single magnetic flux surface is divided among the magnetic flux surfaces which the fast ions created at each mesh point move across in proportion to the fraction of bounce time, W_{ij}, defined by Eq. (31); the same calculation is performed for all mesh points on all magnetic flux surfaces. The total fast ion birth rate on a single magnetic flux surface is given by summing the divided birth rates calculated on the related magnetic flux surfaces.

The typical CPU time for calculating the fast ion deposition profile in Doublet III within a computational error of 10% over the entire range of the minor radius is 10–20 s with the orbit correction and 5–10 s without the orbit correction on the KL DEC-10 computer. This time is shorter by an order of magnitude than that of a Monte Carlo beam deposition code. In order to evaluate the computational model and check the program, we use the parameter A defined by

$$A = \frac{\int_0^a \dot{n}_B(r)\, dV}{N_{\text{in}} - N_{\text{out}}}, \tag{32}$$

where N_{in} is the neutral particle injection rate into the plasma and N_{out} is the outgoing neutral particle rate out of the plasma without suffering any electron loss collisions in the plasma. In principle, A in Eq. (32) must be 1 for all fast ion species. In the calculation described in this section, A is in the range of 1.01–0.96.

3.1. *Fast Ion Deposition Profile*

Figure 5 shows the total fast ion deposition profile in Doublet III. Parameters employed in this calculation are: plasma current, $I_p = 530$ kA, line-averaged electron density, $\bar{n}_e = 5 \times 10^{19}$ m^{-3}, central electron temperature, $T_e(0) = 1.2$ keV, effective charge number, $Z_{\text{eff}} = 1.5$, typical charge number of impurity ions in the plasma, $Z = 8$, central elongation, $\kappa(0) = 1.15$, outward shift of the magnetic axis, $\Delta(0)/a = 5.8 \times 10^{-2}$, neutral beam energy = 80 keV, ion species = 6:3:1 in ion current extracted from an ion source, injection angle, $\theta_1 = 14°$ and $\theta_2 = 4.3°$, and the neutral beam cross-section dimensions, $a_B = 0.15$ m and $\kappa_B = 0.56$. The neutral beam intensity distribution is approximated as the Gaussian distribution. The temperature and density profiles of the plasma are assumed as

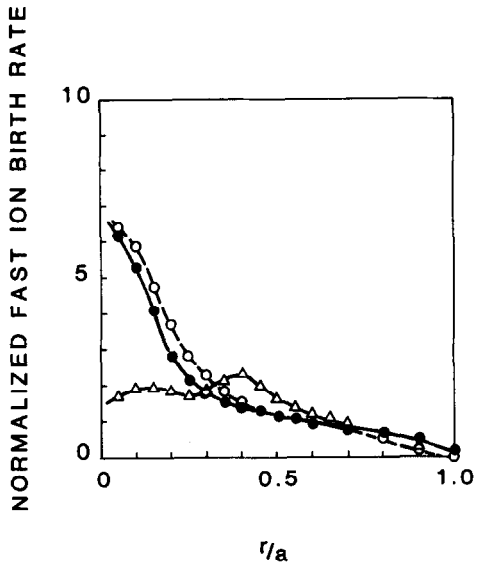

FIG. 5. Normalized fast ion birth rate. ●: without the orbit correction, ○: with the orbit correction in coinjection, △: with the orbit correction in counterinjection.

$$n_j(r) = (n_j(0) - n_j(a)) \left\{ 1 - \left(\frac{r}{a} \right)^4 \right\} + n_j(a), \tag{33}$$

$$T_j(r) = (T_j(0) - T_j(a)) \left\{ 1 - \left(\frac{r}{a} \right)^2 \right\} + T_j(a). \tag{34}$$

In Fig. 5, the total fast ion deposition profiles normalized by the averaged fast ion birth rate with and without the orbit correction for both coinjection and counterinjection are shown. In the case of coinjection, the fast ion birth rate with the orbit correction increases to a maximum of 30% at the inner plasma region and decreases slightly at the outer plasma region compared to the birth rate derived without the orbit correction. The major reason for this phenomenon is that the fast ions created in the outer part of the torus tend to travel inward from the magnetic flux surface on which the fast ions are created and that near the plasma edge the fest ions are lost to the walls due to so-called orbit loss. In the case of counterinjection, the fast ion birth rate with the orbit correction decreases significantly around the central region of the plasma because the fast ions tend to travel outward.

3.2. *Comparison with the Monte Carlo Code*

In order to evaluate the model for the orbit correction employed in the present code and estimate the spatial diffusion of the fast ions during the slowing down due to pitch angle scattering, we have compared the fast ion and the power deposition profiles calculated by the present code with those calculated by the Monte Carlo code [12] which was developed to calculate the complete behaviors of the fast ions in

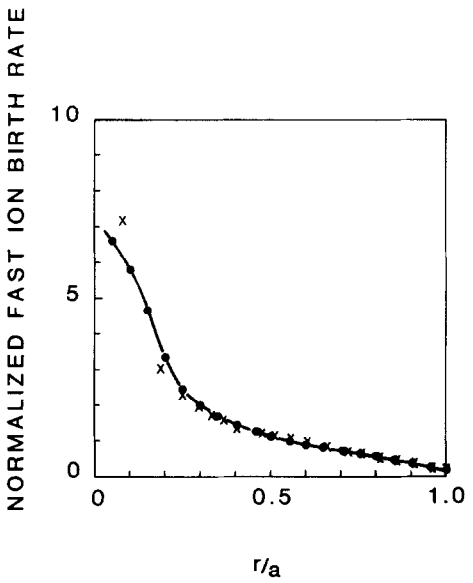

FIG. 6. Comparison of the fast ion birth rate calculated by the present code with that given by the Monte Carlo code [12]. ●: the present code, ×: the Monte Carlo code.

circular plasmas including the pitch angle scattering, orbit loss, and charge exchange loss with reionization. In this comparison, the charge exchange process is excluded because the present code is not capable of calculating the behaviors related to the charge exchange process.

Figure 6 shows the fast ion deposition profile which is the starting point for calculating the power deposition profile. The fast ion deposition profiles calculated by both codes are in good agreement except in the region $r/a < 0.1$. This discrepancy in the central region is caused by the divergence due to the pencil beam approximation which is used in the Monte Carlo code.

Figure 7 shows the power deposition profile to the plasma ions normalized by the average energy transport rate. In the present code, the power transported to the ions from the fast ions is calculated by means of an analytical solution of the Fokker–Planck equation [13]. The power deposition profile with the orbit correction calculated by the present code is in good agreement with that calculated by the Monte Carlo code except for the central region. This agreement shows that the assumption of neglecting the spatial diffusion of the fast ions due to pitch angle scattering during the slowing down is quite reasonable and also proves that the orbit correction is taken into account in a reasonable manner in the present code.

3.3. *Orbit Effect*

In order to estimate the orbit effect on the power deposition, the volume integrated power, $P_{\mathrm{abs}}^{a/2}$, transported to the plasma inside the minor radius of $r/a \leqslant 0.5$ is

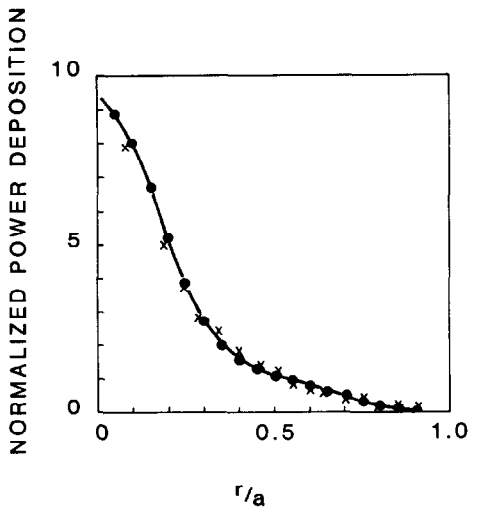

FIG. 7. Comparison of power deposition profile calculated by the present code with that given by the Monte Carlo code. ●: the present code, ×: the Monte Carlo code.

calculated in both cases with the orbit correction in coinjection and without. Figure 8 shows the parameter dependence of $P_{abs}^{a/2}$ on the plasma current, I_p, for each fast ion species. All other parameters are those in Fig. 5. The vertical axis of Fig. 8 represents the variation rate of $P_{abs}^{a/2}$, $(P_1 - P_0)/P_0$, where P_1 and P_0 are $P_{abs}^{a/2}$ with and without the orbit correction, respectively. The total $P_{abs}^{a/2}$ with the orbit correction increases 10% – 15% and the variation rate, $(P_1 - P_0)/P_0$, decreases with the plasma current. This result is reasonable because the shift of the fast ion drift orbit and the banana width depend on the poloidal Larmor radius of the fast ion. However, Fig. 8 also shows that $(P_1 - P_0)/P_0$ increases with the decrease of fast ion energy in the same plasma current although the poloidal Larmor radius increases with the fast ion energy. The reason for this tendency is that the deposition profile of the low energy fast ions of which a relatively large amount are created near the plasma edge region is affected strongly by the orbit effect since in coinjection fast ions tend to travel inward as described in Section 3.1. Figure 9 illustrates the electron density dependence of $(P_1 - P_0)/P_0$ at $I_p = 700$ kA. All other parameters are those in Fig. 8. $(P_1 - P_0)/P_0$ increases with the electron density due to the fact that at high density a relatively large amount of fast ions are created near the plasma edge region. Consequently, at high electron density and low plasma current, the variation of $P_{abs}^{a/2}$ due to the orbit effect increases up to 20%–30% in Doublet III. Thus, using these plasma parameters, it is important in the transport analysis of beam heated plasmas to take the orbit effect into account.

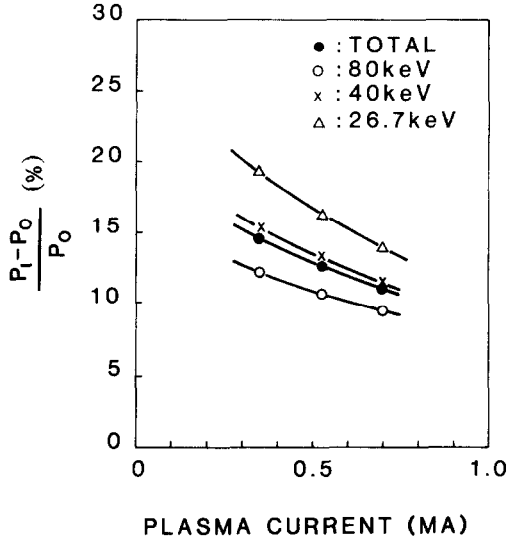

FIG. 8. Plasma current dependence of the variation rate of $P_{abs}^{a/2}$ due to the orbit effect. $P_{abs}^{a/2}$ is the power transported from the fast ions to the plasma inside the minor radius of $r/a \leqslant 0.5$.

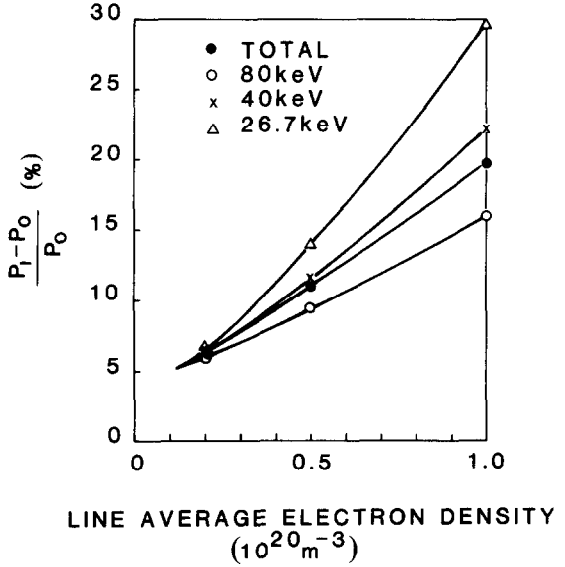

FIG. 9. Line-averaged electron density dependence of the variation rate of $P_{abs}^{a/2}$.

4. Summary

A new neutral beam deposition code has been developed which has the following capabilities:

(1) The new code is capable of calculating the fast ion deposition profile injected into non-circular plasmas with a variable elongation and an outward shift of the magnetic flux surface.

(2) A neutral beam injection with an arbitrary injection geometry can be considered.

(3) The orbit correction for a fast ion deposition profile is considered by weighting each fast ion birth rate by the fraction of bounce time which the fast ion spends in the related differential volume between the magnetic flux surfaces.

(4) Typical CPU time on the KL DEC-10 computer for calculation of a fast ion deposition profile in Doublet III is 10–20 s with the orbit correction and 5–10 s without the orbit correction. This time is shorter by an order of magnitude than that of a Monte Carlo beam deposition code.

The computational results in Doublet III show:

(1) The fast ion birth rate with the orbit correction increases in coinjection and decreases in counterinjection in the area of the plasma center compared to the fast ion birth rate without the orbit correction.

(2) In the case of coinjection, the volume integrated power transported to the plasma inside the minor radius of $a/2$ increases 10%–20% due to the orbit effect.

(3) This increment increases with the decrease in plasma current and also increases when a relatively large amount of fast ions are created near the plasma edge region since fast ions tend to travel toward the central region of the plasma. Thus, the increment increases with electron density and decreases with beam energy.

(4) The power deposition profile calculated by the present code is in good agreement with that calculated by the Monte Carlo code which is able to describe the complete behavior of fast ions in the plasma. This agreement shows that the orbit correction is taken into account in a reasonable manner in the new code.

The code can easily be modified to allow calculation of the fast ion deposition profile for plasmas having triangularity of the magnetic flux contour.

Acknowledgments

The authors would like to express their gratitude to K. Shinya for his help in calculating the plasma equilibrium in Doublet III. The authors would also like to thank the members of the JAERI team at Doublet III, M. Yoshikawa and S. Mori for their continuing encouragement throughout this work. The authors would also like to thank T. Ohkawa and the staff of the General Atomic Company for their support.

REFERENCES

1. D. W. SWAIN, M. MURAKAMI, S. C. BATES, *et. al.*, *Nucl. Fusion* **21** (1981), 1409.
2. D. MEADE, *et. al.*, *in* "Plasma Physics and Controlled Nuclear Fusion Research" (Proc. 8th Int. Conf. Brussels, 1980), Vol. 1, p. 665. IAEA, Vienna, 1981.
3. N. SUZUKI, JFT-2 group, 10th European Conference on Controlled Fusion and Plasma Physics, 1981, Moscow.
4. A. COLLERAINE, *et. al.*, "Preliminary Neutral Injection Experiments on Doublet III," 3rd Joint Varenna-Grenoble Int. Symp. on Heating in Toroidal Plasmas, 1982, Grenoble.
5. J. A. ROME, J. D. CALLEN, AND J. F. CLARKE, *Nucl. Fusion* **14** (1974), 141.
6. R. H. FOWLER, J. A. HOLMES, AND J. A. ROME, Oak Ridge National Laboratory Report, ORNL/TM-6845, 1979.
7. M. NAGAMI, H. YOKOMIZO, M. SHIMADA, *et. al.*, *Nucl. Fusion* **22** (1982), 3.
8. F. W. MCCLAIN AND B. B. BROWN, "GAQ—A Computer Program to Find and Analyze Axisymmetric MHD Plasma Equilibria," General Atomic Co. Report GA-A14490, 1977.
9. A. C. RIVIERE, *Nucl. Fusion* **11** (1971), 363.
10. R. E. OLSON, *et. al.*, SRI Annual report, MP-77-59, 1977.
11. F. H. TENNEY, "Confinement of Energetic Alphas in TCT and Tritons in PLT," Princeton Plasma Physics Laboratory Report MATT-1132, 1975.
12. K. TANI, M. AZUMI, M. OTSUKA, *et. al.*, Proc. Joint Varenna-Grenoble Int. Symp. Heating in Toroidal Plasmas, Grenoble 1 (1978), 31.
13. J. D. CALLEN, R. J. COLCHIN, *et. al.*, *in* "Plasma Physics and Controlled Nuclear Fusion Research" (Proc. 5th Int. Conf. Tokyo, 1974), Vol. 1, p. 645, IAEA, Vienna, 1975.